Materials and Design 194 (2020) 108841

Contents lists available at ScienceDirect

Materials and Design

journal homepage: www.elsevier.com/locate/matdes

Concurrent geometry- and material-based process identification and optimization for robotic CMT-based wire arc additive manufacturing

Thomas Lehmann [a], Akshay Jain [a], Yash Jain [a], Henriette Stainer [d], Tonya Wolfe [b], Hani Henein [c], Ahmed Jawad Qureshi [a,*]

[a] *Department of Mechanical Engineering, University of Alberta, Edmonton, AB, Canada*
[b] *InnoTech Alberta, Edmonton, AB, Canada*
[c] *Department of Chemical and Materials Engineering, University of Alberta, Edmonton, AB, Canada*
[d] *Department of Interdisciplinary Engineering, University of Sheffield, Sheffield, United Kingdom*

HIGHLIGHTS

- Process parameters influencing the geometrical, mechanical and metallurgical consistency are identified and optimized
- A parameter combination is found optimizing the quality of single-track wall benchmark components made from low-carbon steel
- Correlations are found between accumulated heat during fabrication and geometrical variations of the benchmark components
- Correlations between microstructure variations and geometrical variations are found

GRAPHICAL ABSTRACT

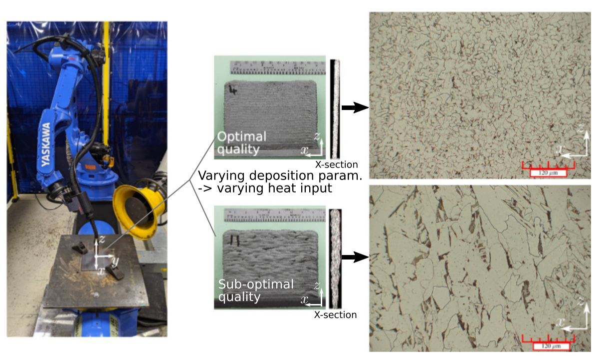

ARTICLE INFO

Article history:
Received 4 February 2020
Received in revised form 11 April 2020
Accepted 30 May 2020
Available online 10 June 2020

Keywords:
Process identification
Process response optimization
WAAM
CMT
Robotic additive manufacturing

ABSTRACT

Additive Manufacturing (AM) is a novel manufacturing method where a component is fabricated by accumulating material layer-by-layer therefore facilitating customized near-net-shape components while maximizing design freedom. A metal AM technology suited for large-scale component fabrication that has been emerging in recent years and is commonly referred to as Wire and Arc AM (WAAM) uses Gas Metal Arc Welding (GMAW) technology to deposit material and large-scale robotic serial manipulator systems (reach >1 m cubed). One of the requirements for applying GMAW welding technology to AM is to identify and optimize deposition parameters in order to achieve a desired deposition quality measured in terms of geometrical, mechanical and metallurgical consistency. In this work, deposition process parameters qualitatively and quantitatively influencing the geometrical, mechanical and metallurgical consistency are identified and statistically validated. A deposition parameter combination is found that optimizes the quality of single-track wall benchmark components made from low-carbon steel. Moreover, correlations are found between accumulated heat during fabrication and the geometrical variations of the benchmark components due to bead slumping. Additionally, correlations between microstructure variations and geometrical variations are found. Finally, based on the presented analyses, in-situ temperature monitoring methods are proposed in order to achieve optimal component quality.

* Corresponding author at: 10-361 Donadeo Innovation Centre for Engineering, 9211-116 Street NW, Edmonton, AB T6G 1H9, Canada.
E-mail addresses: lehmann@ualberta.ca (T. Lehmann), ajain2@ualberta.ca (A. Jain), yjain@ualberta.ca (Y. Jain), hstainer1@sheffield.ac.uk (H. Stainer), Tonya.Wolfe@innotechalberta.ca (T. Wolfe), hhenein@ualberta.ca (H. Henein), ajquresh@ualberta.ca (A.J. Qureshi).

https://doi.org/10.1016/j.matdes.2020.108841

1. Introduction

According to the American Society for Testing and Materials (ASTM), Additive Manufacturing (AM), or 3D printing, is a manufacturing methodology where material is accumulated layer-by-layer, as opposed to cutting away material as in traditional manufacturing (subtractive) [1]. Owing to this accumulative method, the most prevalent advantage of AM is the possibility to manufacture highly optimized and customized near-net-shape components while minimizing design constraints. This allows for entirely novel design strategies where the component geometry can be optimized to reduce weight and material usage while at the same time maintaining equivalent mechanical properties such as tensile and compressive strength compared to components manufactured with subtractive manufacturing. While various materials such as polymers, ceramics, composites and metals can be considered for AM the focus of this work is on metal AM.

Currently, the most common and also commercialized metal AM technology is Powder Bed Fusion (PBF) [2–4] where layers of metal powder are selectively molten or sintered via directed high-power laser light. Once desired areas of a layer have solidified, a new layer of metal powder is applied followed by selectively melting. While PBF has proven to produce high-quality functional components for safety-sensitive applications such as the aerospace industry, some limitations exist. PBF is limited to 2.5 degrees of freedom (DOF) printing meaning that the vertical coordinate is incremented in discrete steps according to the desired height of each layer. A necessary requirement for 2.5 DOF printing is that support structures are needed for overhanging features, which can impose significant limitations on component design [5]. A second restriction of PBF is the limited size of the build volume since, a scale up of PBF involves prohibitively non-linear increase in the powder needs and corresponding increase in support structure.

PBF has clearly shown to be suitable for many small-scale applications and will remain to be an important metal AM technology. However, owing to the above mentioned limitations of required support structures and limited component size, other methods for large-scale and scaleable metal AM are currently explored. An emerging alternative metal AM technology is based on gas metal arc welding (GMAW) deposition technology and is now commonly known as wire-and-arc AM (WAAM) [7,8,16–20]. Another commonly found arc-based deposition technology suitable for welding-based metal AM is gas tungsten arc welding (GTAW) [21–27]. The focus of this work is, however, on GMAW-based WAAM. One variant of GMAW–*Cold Metal Transfer* (CMT)–which was first developed by Fronius International GmbH for joining dissimilar metals in the automobile industry, has gained popularity in recent years in WAAM research due to the significantly reduced heat input [10,12,28–33]. Among other advantages, the lower heat input results in an improved bead profile and therefore smoother 3D component's surfaces and is achieved by reducing and controlling the current during the short-circuit phase while at the same time retracting the wire to enhance droplet transfer [34].

In order to achieve large-scale printing volumes of >1 m^3, in recent years, systems where large-scale robotic manipulators carry the welding torch have been proposed [6,15,20,35,36]. In many cases, these robotic systems are augmented with positioning systems allowing for tilting and rotating of the component as it is fabricated [37,38] (see Fig. 1). The use of a positioning system for re-orienting the component during fabrication enables multi-directional deposition and therefore eliminates the need for support structures as the direction of material deposition can be re-aligned such that overhanging component features can be printed in alignment with the gravity vector.

A requirement to utilize GMAW welding technology for AM is to identify system parameters and parameter envelopes within which the geometry (size, shape) and quality of the deposited bead can be influenced and optimized, which in turn allows for control of the geometry and geometric quality of 3D components. When viewed from a system identification perspective, the system consists of various input parameters, which influence system responses such as the bead geometry. Among the fundamental input parameters reported in the literature are the wire feed speed (WFS), welding current and voltage, and torch travel speed (TTS) [7,8,18]. Welding current and voltage are coupled to the WFS and influence the thermal energy input into the system. Depending on the balance between applied and extracted heat (primarily through conduction through the plate and convection of the build), thermal energy can accumulate, which can significantly influence the solidification rate and therefore the bead geometry. It has been reported by Lu et al. that excessive heat accumulation can lead to deteriorating layer forming quality [13], which can lead to collapsing layers due to insufficient solidification [14]. Other researchers found experimentally and through simulation that the temperature gradient in the melt pool decreases as layers and therefore heat in the component accumulate [39,40]. In order to mitigate the issue of heat accumulation, Montevecchi et al. proposed increased convective heat transfer through air jet impingement [41] and also propose an FEM-based method for inter-layer dwell time computation [42].

1.1. Related work and contribution

Various contributions have been made in the past 15 years on deposition parameter and system identification. Literature related to this work is reviewed chronologically in the following paragraphs. Moreover, a listing of studies investigating process parameters and their responses is provided in Table 1.

Dickens et al. were the first to explore the suitability of GMAW welding to fabricate 3D components layer-by-layer using a constant voltage (CV) GMAW power supply and mild steel wire to deposit single-bead welds. It was concluded that the bead geometry can be controlled by adjusting parameters such as voltage, WFS, wire stick-out (WSO), wire diameter and TTS. However, details on parameter significance were not provided [6]. Song et al. provided an investigation of the main deposition-related process parameters, their optimization and influence on the system response when using mild steel (AWS 5.18 70S-6) with a CV GMAW power supply. It was found through a Taguchi design of experiments (DOE) that welding voltage and WFS contribute heavily to both spatter formation and bead width while parameters such as WSO and the shielding gas composition have negligible effects [7]. Kazanas et al. presented an experimental study using a CMT power supply and mild steel where the quality of straight, single-track walls was assessed in terms of effective wall thickness (EWT) and the surface waviness (SW). The results established a relationship between TTS, WFS and EWT and show that the wire diameter has only a minor influence on the SW [8]. A further study on the key factors influencing the forming appearance of single-track walls of 180 mm length and seven layers height fabricated by a CV power supply and steel wire was proposed by Xiong et al. The authors found that the heat input is dependent on the WFS and TTS and that excessive heat input negatively influences forming appearance for currents exceeding 200 A [9]. Prado-Cerqueira et al. conducted a further study on the relation between welding parameters and the geometry of single-track, single-layer beads while also utilizing a CMT welding power supply and steel wire. While considered parameters were the TTS, welding current, arc correction and dynamic correction, results show that the bead geometry is mainly a function of the welding current and therefore the WFS, where higher current increases the bead width by a larger margin than the bead height [10]. Liberini et al. conducted an experimental study with emphasis on the effect of process parameters on the microstructure of 15-layer single-track walls fabricated with a CV GMAW power supply (Millermatic 300), steel wire and using a 60 s dwell time between layers. The authors concluded that there are no substantial microstructure differences across trials when adjusting voltage and TTS likely due to the limited variation in heat input. Furthermore, three different microstructure zones were identified in each sample due to the varying thermal history [11]. Gonzalez et al. continued the work of

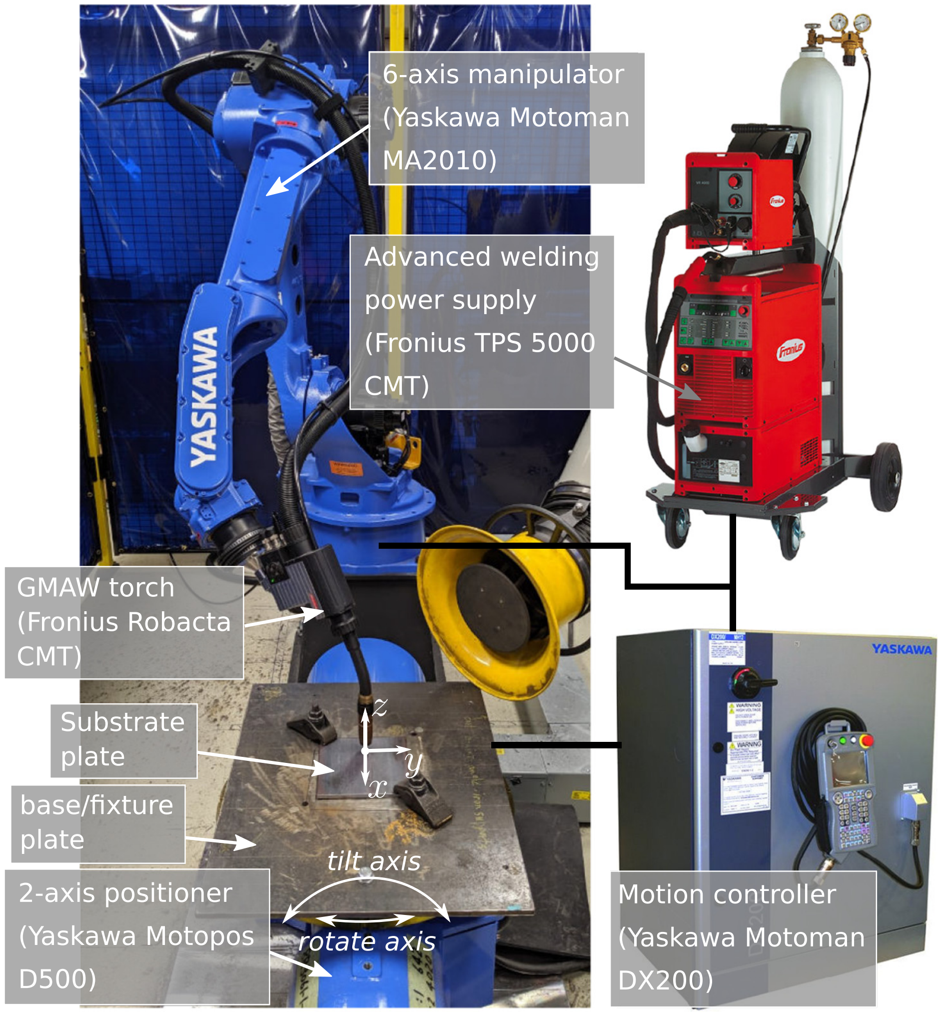

Fig. 1. The large-scale 8-axis robotic WAAM system used for the experimental studies presented in this work. The system consists of a 6-axis manipulator and a 2-axis tilt-rotate positioner. A Fronius Robacta CMT torch is mounted on the tool flange of the manipulator and operated by a Fronius TPS 5000 CMT welding power supply, which is fully integrated with the robotic system's motion controller.

Table 1
A listing of studies investigating the influence of process parameters on various responses.

Reference	Material	Deposition technology	Variable process parameters	Observed process responses
Dickens et al. [6]	Steel	CV[a] GMAW	TTS[b], WFS[c], U[d], WSO[e], wire diameter	Bead width, height
Song et al. [7]	Steel	CV GMAW	WFS, U, WSO, shielding gas	Bead width, weld spatter
Kazanas et al. [8]	Steel	CMT[f]	TTS, WFS, wire diameter	EWT[g], SW[h]
Xiong et al. [9]	Steel	CV GMAW	TTS, I[i]	Layer formation, heat input
Prado-Cerqueira et al. [10]	Steel	CMT	TTS, I, AC[j], DC[k]	Bead width, height
Liberini et al. [11]	Steel	CV GMAW	TTS, U	Microstructure, microhardness
Gonzalez et al. [12]	Steel	CMT	TTS, I, AC, DC, number of layers	Wall width, height, SW, layer height deviation, growth per layer
Yang et al. [13]	Steel	CV GMAW	Dwell time	Temperature, SW, wall height
Lu et al. [14]	Steel	CV GMAW	TTS, WFS, U, WSO, substrate cooling method	Bead width, height, microstructure, tensile strength
Martina et al. [15]	Steel	Pulsed GMAW (tandem)	TTS, WFS	Microstructure, hardness

[a] Constant voltage.
[b] Torch travel speed.
[c] Wire feed speed.
[d] Voltage.
[e] Wire stick-out.
[f] Cold metal transfer.
[g] Effective wall thickness.
[h] Surface waviness.
[i] Current.
[j] Arc correction.
[k] Dynamic correction.

Prado-Cerqueira et al. [10] to further study the optimal process conditions for the CMT welding process for single-track walls with a varying amount of layers using steel wire and adjusting arc length correction, dynamic correction, TTS and welding current. Results showed a decreasing layer height with increasing amount of layers, likely due to heat accumulation, which leads to slumping and that varying the welding current from 40 A to 65 A does not significantly influence surface roughness [12]. Yang et al. investigated the influence of inter-layer dwell time on the heat accumulation within twenty-layer single-track walls using a CV GMAW power supply and steel wire. It was shown experimentally that higher inter-layer dwell time improves the forming quality (e.g., surface waviness) of the single-track wall [13]. Lu et al. published a study where the process parameters were analyzed with respect to the influence on weld bead geometry of single-track and single-layer, and single-track multi-layer deposition using a CV GMAW power supply and mild steel wire. The single-bead and single-layer deposition trials indicated that the bead geometry is mainly controlled by the voltage, TTS and WFS while the WSO only influences the bead quality while the single-track and muti-layer trials showed that through compulsory cooling (active water-cooling) and therefore increased heat extraction, slumping and collapsing of layers due to excessive heat accumulation can be avoided [14]. Martina et al. studied the feasibility of the tandem pulsed GMAW welding process of increased material deposition of 17-4 pH stainless steel onto an actively cooled substrate plate. The authors carried out experiments to study the effect of WFS and TTS on the quality of single-track walls and found that a WFS up to 7 m/min are possible with a TTS of 1.2 m/min. The change in hardness for increasing WFS was found to be insignificant [15]. Ali et al. studied the use of hot work tool steel in terms of process technology and metallurgy. It was found that a layer width range of 2.7–9.4 mm can be achieved, near-net-shaped structures with equal layer width can be achieved and mechanical properties can be adjusted through the energy input and thermal field with active cooling of the substrate plate [43].

The most commonly considered input parameters in the above reviewed relevant literature are TTS (9), WFS (6), WSO (4) and current (3). These parameters have also been found to have the most significant influence on the system responses such as bed/layer geometry/morphology/topometry (7), and microstructure (3). Particularly TTS and WFS significantly influence the bead geometry [7,8,14,15,36], which is an intuitive conclusion as the combination of WFS and TTS controls the amount of deposited material per unit distance.

A limiting factor associated with the adjustment of the bead geometry through the combination of TTS and WFS, however, is the amount of heat introduced into the component where the higher the wire feed speed, the more heat is introduced. This fact imposes a limit onto the possible size of the bead if the heat can not be extracted sufficiently. The accumulating heat causes slumping of beads due to a reduced solidification rate as the layers are stacked such that layer width and height becomes inconsistent [9,12–14]. This gradual change in solidification rate and varying heating cycles can then also lead to variations in microstructure throughout the component [11,14]. In order to reduce the amount of heat input over time, the most frequently explored solution is the addition of a dwell time after the deposition of each layer [11,13].

While some work on parameter identification and optimization has been done, it is apparent from the above provided literature review that a thorough investigation of the CMT process in terms of process quality optimization while considering effects of heat accumulation on the component geometry, microstructure, and mechanical properties such as hardness is not available. In this work, first parameters of the CMT WAAM process and their quantitative values are investigated and identified through a Design of Experiments (DOE) in order to obtain significant parameters and to find parameter value combinations that yield optimal quality of a fabricated benchmark component. The benchmark component is a single-track wall and the considered quality measure is the deviation of the wall width from the base wall width after fabrication. The chosen process responses are in alignment with the literature where particularly accumulating heat is often cited as having a negative influence on the desired outcome of fabricated components.

Moreover, the influence of the accumulated heat during fabrication of the benchmark component with varying process parameters is analyzed and correlated to the consistency of wall width. Finally, it is analyzed whether there are correlations between microstructure and hardness variations, and the wall width deviation. If these relationships exist, then through minimizing the wall width deviation in-situ, microstructure and hardness variations will also be minimized and the overall quality of the component is ensured.

In summary, the main contributions of this work are the identification of relevant deposition-related parameters and their optimization, metallurgical analyses of fabricated benchmark components, and the establishment of relationships between metallurgical variations, the geometric quality and variations in heat accumulation during fabrication of the benchmark component. The provided studies and analyses will provide a detailed insight into the CMT-based WAAM process and the factors that have a significant influence on the quality of a component fabricated through CMT-based WAAM.

The paper is organized as follows. In Section 2, the experimental robotic large-scale WAAM system is introduced along with the integrated welding system, materials and system settings used for all experimental studies. Subsequently, in Section 3, the performed experimental studies are described and results and analyses presented. First, the parameter envelopes identified during a pilot study are presented followed by the various analyses of a Taguchi DOE on the deposition parameter significance, and mechanical, metallurgical and geometrical variations. Finally, in Section 4, the analysis results are discussed and in Section 5, conclusions and future work are outlined.

2. Robotic WAAM platform & experimental setup

A robotic welding platform is used to deposit vertical single-track, multi-layer benchmark components. The platform consists of an industrial 6-axis serial manipulator (Yaskawa Motoman MA2010), a 2-axis positioner (Yaskawa Motoman Motopos D500), a Fronius TransPuls Synergic 5000 CMT welding power supply, a Fronius VR 7000 CMT wire feeding unit and a Fronius Robacta CMT torch mounted on the manipulator's tool flange. The platform is shown in Fig. 1. The Fronius welding system is fully integrated with the manipulator and positioner's motion controller (Yaskawa Motoman DX200) such that programming of motion and operation of the welding power supply can be fully controlled by the controller's programming pendant.

During all experiments presented in this work, the operation mode of the Fronius power supply is set to CMT. In this operating mode, the welding power supply automatically adjusts the welding current and voltage based on the given WFS via a pre-programmed look-up table stored on the power supply. It should therefore be noted that any modifications of the WFS during experiments described in this work also causes a change in welding current/voltage and therefore the thermal energy introduced into the component. This relation between WFS, current and voltage is often referred to as a synergic line that is unique to a given filler material type and shielding gas mix. The steel wire type used for all experiments was a standard AWS ER70S-6 with a diameter of 1.2 mm, with a nominal chemistry found in Table 2. The shielding gas was a 75% Argon and 25% CO_2 premix at a gas flow of 40 cubic feet per hour (CFH). Accordingly, synergic line number 1220 (Steel ER 70 S-3/6 $ArCO_2$) was set on the welding power supply.

Fig. 2 illustrates two chosen tool paths traversed by the torch nozzle during the fabrication of single-track walls including path sections where the arc is turned on or off. The tool path shown in Fig. 2a was chosen for the pilot experiments detailed in Section 3.1 and the one shown in Fig. 2b was chosen for the Taguchi DOE presented in Section 3.2. The two deposition strategies differ in that during the first strategy, material is only deposited from the start to the end position whereas during the second strategy, a layer is deposited during torch motion in each

Table 2
The nominal chemical composition of standard AWS ER70S-6 welding wire.

Alloying element	C	Mn	S	Si	P	Cu	Cr	Ni	Mo	V
wt%	0.09	<1.60	0.007	0.9	0.007	0.20	0.05	0.05	0.05	0.05

direction, first from the wall start point to the end point and then from the end point to the start point. The reason for utilizing two different deposition strategies for each set of experiments will be further elaborated on in the following sections.

The orientation of the torch nozzle was kept vertical (1G welding position)–in alignment with the *z*-coordinate–during all experiments as shown in Fig. 1.

3. Experimental studies

In this section, analyses of single-track wall benchmark components fabricated with the robotic platform introduced in Section 2 and based on a Taguchi DOE are provided. The experiments are designed for the purpose of exploring the relationships and correlations between process parameter variations and the consistency of the wall width deviation and corresponding metallurgical, mechanical and thermal variations.

3.1. Pilot experiments

In order to determine a reasonable range of parameter values, a set of pilot experiments was conducted where each trial consisted of depositing single-track walls of 10-layer height and a length of 100 mm. The results of these experiments serve to inform the Taguchi DOE so that the required amount of trials can be reduced while maintaining a sufficient parameter envelope. The choice of parameters influencing the outcome of the single-track wall deposition was informed by the previously published studies reviewed in Section 1.1 where it was concluded that WFS and TTS have the most significant influence on relevant responses such as layer/bead geometry and heat input. Other parameters such as the dynamic correction and arc length correction were

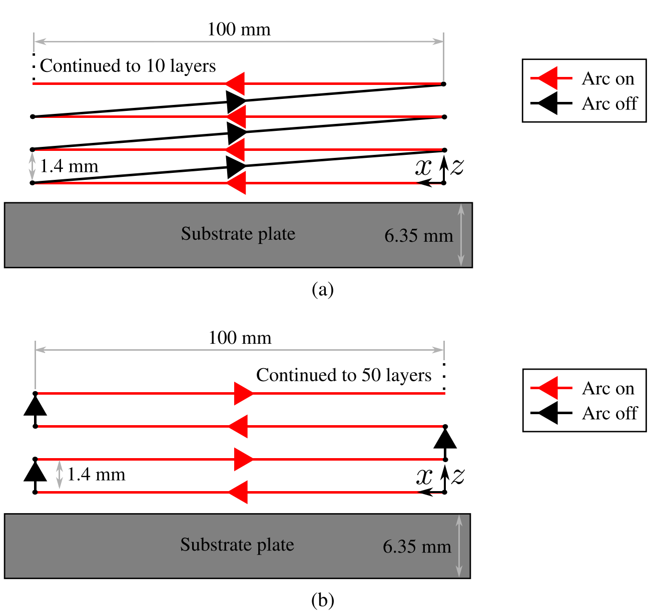

Fig. 2. Schematic representations of the torch path for a single-track multi-layer benchmark components. a) One-directional deposition used for the pilot experiments and b) bi-directional deposition used for the final experiments.

kept constant at zero across all trials. The torch was displaced in *z*-direction by 1.4 mm after each layer. This was empirically determined to be a suitable increment in order to ensure a constant WSO. As mentioned in Section 2, the deposition strategy depicted in Fig. 2a was used for the pilot experiments.

The fabricated single-track walls were assessed visually with emphasis on the quality of each sample. Quality is evaluated with respect to layer slumping, wall surface waviness and wall thickness consistency. The most relevant information to be concluded from this set of experiments is the set of maxima and minima for the considered set of parameters TTS and WFS. The set of pilot experiments including adjusted parameter values for TTS and WFS, and the level of quality are listed in Table 3. In the case where gaps are present in the sample–as shown in Fig. 3, sample 1–due to low wire feed speed, the sample is marked as “defect” in Table 3. It can be observed that at the minimum WFS of 1.27 m/min, defects occur with both sample number 1 and 9 at 0.41 m/min and 0.36 m/min TTS, respectively, meaning that a WFS of 1.52 m/min is the minimum achievable for the chosen reasonable TTS range of 0.30–0.41 m/min. The maximum WFS was 3.81 m/min at a TTS of 0.41 m/min. At this relatively high WFS, there is significant heat input into the component, which manifests in excessive slumping of the layers as shown in Fig. 3, Sample 3. While WFS values of 2.29 m/min exhibit less slumping, it is still moderate to significant. Moreover, a trend can be observed where slower TTS values–0.36 and 0.30 m/min–result in a better average quality than 0.41 m/min. The combination with the best quality was sample number 15–shown also in Fig. 3–where no slumping occurs, the wall surface is very even and the wall thickness is very consistent.

3.2. Taguchi design of experiments

Based on the results of the pilot experiments, the parameter value range for the Taguchi DOE was chosen as follows: WFS = [1.52 2.29] m/min and TTS = [0.30 0.38] m/min and increments of 0.25 m/min and 0.025 m/min, respectively. This particular range for the WFS was chosen because it was observed that outside of this envelope, either incomplete continuous fusion or excessive slumping can occur.

Two additional factors–the dwell time (DT) and amount of stacked substrate plates (SSP)–were added to the set of factors where DT is defined as a waiting period after a layer is deposited. The DT was added as a measure to adjust the thermal input as previously proposed in the literature [11,13]. The SSP (see Fig. 4 for illustration) was added in order to increase the heat sink of the substrate plate therefore enhancing the extraction of heat from the single-track wall. The size of all substrate plates was 152.4×152.4×6.35 mm. The chosen range for the DT was 0–15 s in 5 s increments and for SSP it was two levels (1 or 2 substrate plates stacked). In order to reduce the amount of experiments from a full factorial design of 128 experiments, the Taguchi DOE approach was used, in particular the $L16(2^6),(4^3)$ mixed-level design was utilized and only columns 1–4 of the resulting 16×9 matrix were considered for this experiment design (see Table 4).

As mentioned in Section 2, the bi-directional deposition strategy outlined in Fig. 2b was used as opposed to one-directional deposition strategy used for the pilot experiments. This was done in order to balance out the additional amount of material being deposited at the start of a bead due to gradual increase in torch motion at arc ignition. As evident in Fig. 3 when fabricating a single-track wall using the one-directional deposition strategy, material will accumulate on the start side of the wall leading to the formation of a bulge while the decreased deposition at the end of the wall causes a lack of material deposition. This can be moderated by controlling the WFS and TTS ramp up, but was found the problem was easily solved with the bi-directional strategy as the excessive initial mass flow was balanced out on each end. A further reason for using the bi-directional deposition strategy illustrated

Table 3
The set of pilot experiments and responses.

Sample number	Input parameters		Response (quality)[a]
	TTS [m/min]	WFS [m/min]	
1	0.41	1.27 (10 V, 60 A)	0
2		2.54 (11.8 V, 90 A)	2
3		3.81 (12 V, 135 A)	1
4		2.29 (10.5 V, 84 A)	2
5		2.03 (10.5 V, 75 A)	2
6	0.36	2.03 (11.4 V, 72 A)	3
7		1.78 (10.8 V, 74 A)	3
8		1.52 (10.3 V, 68 A)	5
9		1.27 (10 V, 65 A)	0
10		2.29 (11.5 V, 85 A)	3
12	0.30	2.29 (11.6 V, 80 A)	3
13		2.03 (10.6 V, 77 A)	3
14		1.78 (10.5 V, 73 A)	4
15		1.52 (10.1 V, 66 A)	5

[a] 0 - defects | 1 - excessive slumping | 2 - significant slumping | 3 - moderate slumping | 4 - minor slumping, nearly consistent wall thickness |5 - good finish, no slumping, consistent wall thickness.

in Fig. 2b is that–as was later realized–the inter-layer dwell time can not be controlled fully–due to the torch moving back to the start point–during deposition when using the one-directional strategy. With the bi-directional strategy, however, this is possible as the dwell time is decoupled from the tool path. After fabrication, each single-track wall sample was sand blasted on one side to remove the oxidation layer formed during fabrication.

3.2.1. Wall width deviation: input parameter effects and significance

First, it is statistically analyzed whether and to which degree input parameters (factors) affect the deviation of the wall width (response). The width of each wall sample is measured by means of image processing through detecting the edge of each sample's cross-section. An example of the image processing sequence is shown in Fig. 5. It should be noted that due to varying deposition rates, the height of the single-track wall samples was not consistent across all samples. In order to equalize this inconsistency in wall height, the maximum evaluation height was limited to 52 mm for all samples. The image processing sequence is as follows:

1. Apply a Gaussian low-pass filter on image (a) to blur the surface of the sample.
2. Apply the Otsu thresholding method on image (b) and set pixels with value below the threshold to zero in order to remove the background.
3. Find the wall contour in image (c); the transition from a non-zero pixel value to a zero pixel value across two vertically adjacent pixels marks the boundary of the wall.

After extracting the contour of the wall samples, a measure for the deviation of the wall width is determined as

$$\mathbf{d} = |\mathbf{a} - \mathbf{b}| - |\mathbf{a}_1 - \mathbf{b}_1| \tag{1}$$

where $\mathbf{a}$ and $\mathbf{b}$ are the vectors containing the contour of the top and bottom edge of the wall, respectively (see Fig. 5d). The vector $\mathbf{d}$ as defined in Eq. (1) provides a deviation of wall width along the

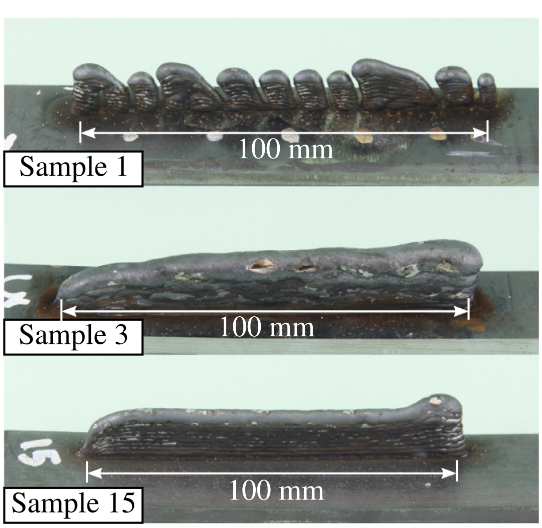

Fig. 3. The three samples 1, 3 and 15.

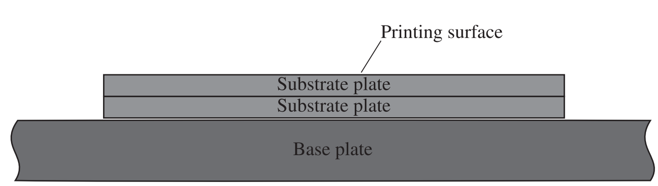

Fig. 4. A schematic illustrating two stacked substrate plates.

Table 4
The set of experiments determined through Taguchi DOE and the response.

Sample number	Input parameters				Response
	WFS [m/min]	TTS [m/min]	Dwell time [s]	SSP[a]	s[b]
1	1.52	0.30	0	1	0.239
2	1.52	0.33	5	1	0.253
3	1.52	0.36	10	2	0.163
4	1.52	0.38	15	2	0.141
5	1.78	0.30	5	2	0.288
6	1.78	0.33	0	2	0.621
7	1.78	0.36	15	1	0.186
8	1.78	0.38	10	1	0.212
9	2.03	0.30	10	1	0.285
10	2.03	0.33	15	1	0.261
11	2.03	0.36	0	2	0.678
12	2.03	0.38	5	2	0.456
13	2.29	0.30	15	2	0.433
14	2.29	0.33	10	2	0.457
15	2.29	0.36	5	1	0.450
16	2.29	0.38	0	1	0.650

[a] The amount of stacked substrate plates.
[b] The wall width deviation expressed as standard deviation s.

length of the wall relative to the width of the wall near the substrate plate. The deviation of wall width **d** is plotted in Fig. 7 for samples 1, 4 and 11.

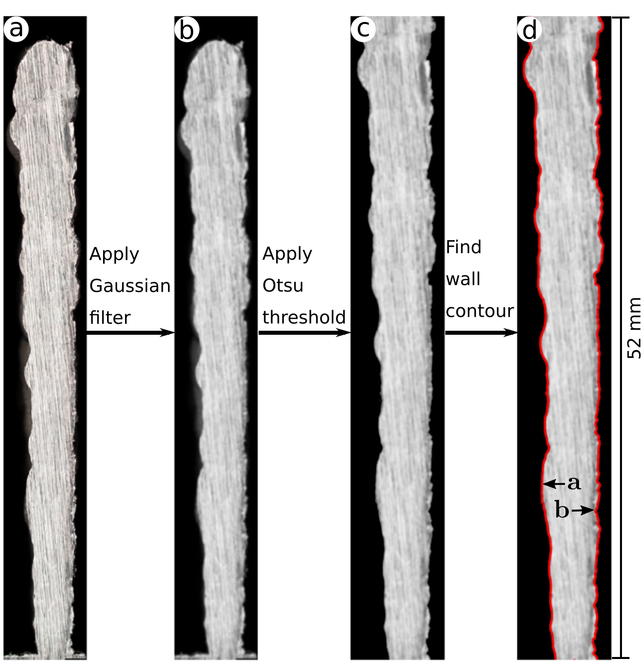

Fig. 5. The image processing sequence for the measurement of sample 16's cross-sectional contour.

In order to obtain a scalar measure for the amount of wall width deviation to be used for statistical analysis, the standard deviation $s = \sqrt{\frac{1}{N-1}\sum_{i=1}^{N}\left(d_i - \overline{d}\right)^2}$ was used where N is the amount of elements in **d**, and $\overline{\mathbf{d}}$ is the mean value of **d**. The standard deviation is chosen as it provides a good measure of the amount of variation contained within **d**.

Fig. 6 shows perpendicular views of single-track wall samples 4 and 11. It can be observed that the quality in terms of surface smoothness and consistency is much better for Sample 4 than that of Sample 11. Fig. 7 plots **d** for the samples 1, 4 and 11. When comparing Sample 4 (least amount of standard deviation) with Sample 11 (most amount of standard deviation), it can be observed that the width deviation varies from <0.5 mm to >2 mm. Fig. 8 plots the standard deviation s of **d** for all 16 samples, obtained as the response on Table 4. The plot clearly shows a much higher standard deviation for the three samples 6, 11 and 16

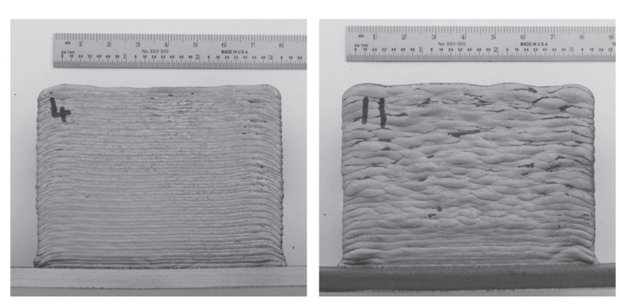

Fig. 6. Two exemplary single-track wall samples. a) Sample 4 and b) Sample 11.

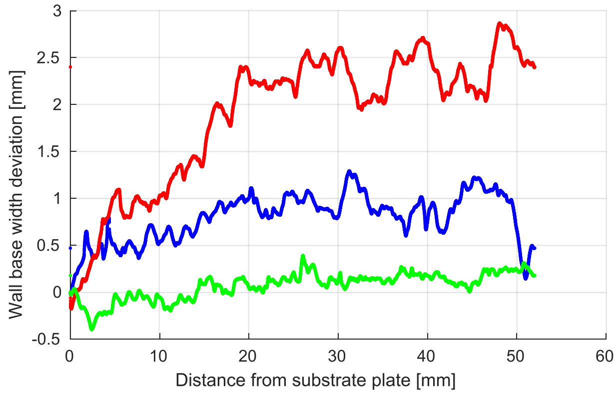

Fig. 7. The deviation of the wall width relative to the base wall width for samples number 1, 4 and 11.

compared to all other samples. All three samples have in common that the DT is zero. Only Sample 1 (also with a DT of zero) does not exhibit the large amount of deviation. This suggests much more slumping and therefore heat accumulation for samples without DT. A further trend that can be observed from Fig. 8 is a steady increase in the standard deviation with increasing WFS across samples with non-zero DT. This indicates a positive correlation between the WFS and the bead slumping where a higher WFS results in a higher amount of bead slumping.

In order to provide rigorous statistical proof for whether there is a significant influence of the input parameters over the response, an Analysis of Variance (ANOVA) was carried out on the data listed in Table 4. The ANOVA results are listed in Table 5. The p-value provided in the table shows that the WFS, DT and SSP have a significant influence on the deviation of the wall thickness s at a confidence of 95%. At a confidence of 99%, only the WFS and DT show a significant influence.

3.2.2. Thermal analysis

In this section, the relationship between the average heat accumulated in a fabricated single-track wall sample and its quality is analyzed. This is done by measuring the surface temperature throughout the fabrication of each single-track wall. During fabrication of each sample, thermal imagery is collected using a Mikron® M7640 infrared (IR) camera and is used for the estimation of average heat in the sample. During fabrication of some samples, unfortunately the recording failed so that only usable image data for samples 1, 2, 5–12, and 15 could be obtained. Along with the following detailed description of the algorithm, Fig. 9 and Algorithm 1 further illustrate the process of computing the average accumulated heat within the component during fabrication.

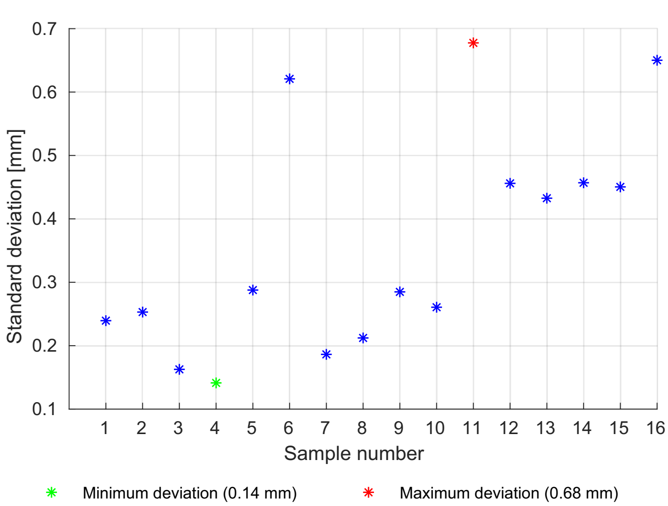

Fig. 8. The standard deviations s of wall width deviation for each single-track wall sample.

Table 5
The ANOVA results.

Source	Sum sq.	DOF	Singular?	Mean sq.	F	Prob>F (p-value)
WFS	0.198	3	0	0.066	19.935	0.0033
TTS	0.016	3	0	0.005	1.589	0.3032
DT	0.210	3	0	0.070	21.174	0.0029
SSP	0.030	1	0	0.030	9.210	0.0289
Error	0.017	5	0	0.003		
Total	0.471	15	0			

The IR video is first converted to a 3-dimensional array, $\mathbf{T}$, of size $A \times R \times C$ where A is the number of frames, R and C are height and width of each frame, respectively. Elements of the array $\mathbf{T}$ specify temperature of every pixel of every frame collected during fabrication of the sample. In order to obtain the average heat accumulated in the sample, first the foreground (sample) is separated from the background using a process called foreground separation. Thus, the essential operation required is the separation of the sample from the moving torch and static temperature background in every frame. Different foreground separation techniques such as subspace learning models, robust principal component analysis models and convolutional neural network models were tried. However, Convolutional Neural Network (CNN) models [44] worked best for this use case due to the dynamic nature of the background (moving torch is also treated as background). As there was no ground truth for the foreground, a pre-trained CNN was used to classify each pixel in every frame as background or foreground. Network architecture and training parameters were kept the same as in [44].

After this, frames are removed from array $\mathbf{T}$ such that only the frames where material is deposited (excluding dwell time) are considered for computation of the accumulated heat.

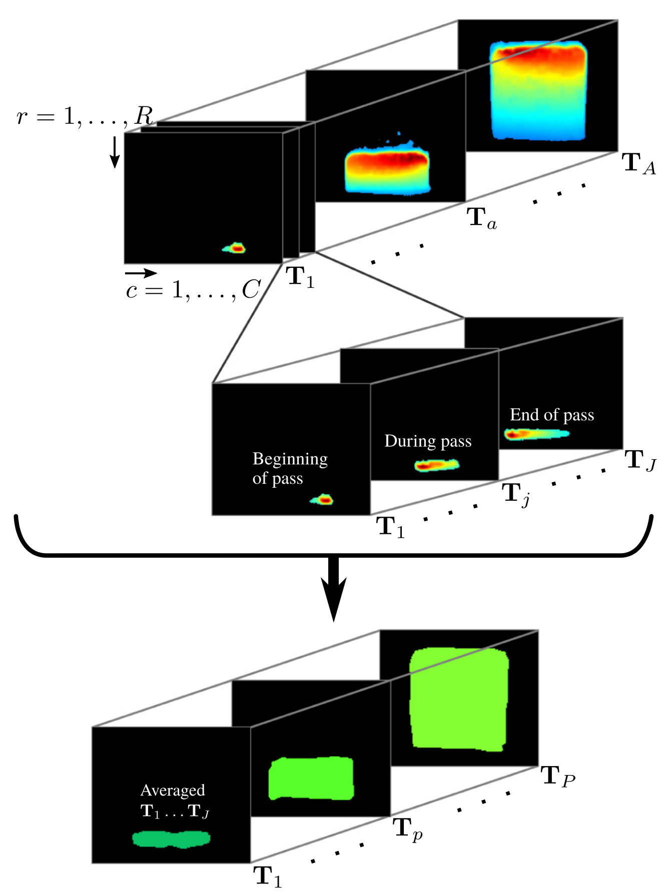

Fig. 9. A flowchart illustrating the computation of the average heat accumulation.

Then, during deposition, the heat signature of the torch, is removed from each frame since the temperature of the point just below the torch is relatively high and, if included, would falsify the computation of the average accumulated heat. In order to do this, all frames contained within a single pass of the torch are averaged therefore minimizing the effect of the torch's heat signature.

The dimension of **T** is now shrunk to $P \times R \times C$ where P is the number of passes (layers). After that, **T** is mapped to a single scalar t by averaging **T** first across layers, P, and then across R and C. Finally, the vector **t** containing t for each sample is normalized to $\mathbf{t}' \in (0,1)$ in order to obtain a dimensionless scalar for the average amount of accumulated heat. This was done because it was not possible to accurately measure the emissivity of each wall sample. The method was deemed appropriate since only the change in accumulated heat is relevant across samples and it can be assumed that the emissivity across all samples is equal. To show whether there exists a correlation between the average accumulated heat in each sample and the the wall width deviation, linear regression was used. Fig. 10 shows the wall width deviation plotted against the normalized accumulated heat including a linear fit onto the data. The p-value of 0.0008 for the regression analysis (average accumulated heat) indicates that there is a significant positive correlation between the wall width deviation and the average accumulated heat. The average heat input was calculated based on the general heat input calculation for welds $Q_{in} = \frac{UI}{TTS}$ where U is the welding voltage and I is the welding current. The data is presented in Fig. 10, with significant scatter and a low quality of fit. By weighting the average heat input with the dwell time, the relationship between heat input and wall width deviation becomes stronger and matches the measured heat. The difference in calculated heat input and measured accumulated heat is the efficiency of the system, which was determined to be 0.74 and in line with the standards set out by EN ISO 1011-1 for heat input calculation. It should also be noted that the power source is waveform-controlled and that the standard calculations are only an approximation of actual heat input. The method of determining the accumulated heat using the IR data is valid as there is good alignment between the experimental and theoretical values.

Algorithm 1. Computation of average accumulated heat.

```
Input: 3D array T containing temperature values
Output: A scalar value t
  procedure COMPUTE_AVERAGE_HEAT(T)
     for each frame in T do
        frame ← BACKGROUND_SEPARATION_CNN(frame)
        if frame recorded in dwell time then
           T.REMOVE(frame)
        end if
     end for
      T is now of size A × R × C
      Let J be the number of frames recorded during a single pass
      Let P be the number of passes
     for p in (1,2, … , P) do
        Compute average T across dimension A
        T[ (p-1)*J : (p)*J ].MEAN(dimension=A)
     end for
      T is now of size P × R × C
      Compute average T across passes P
     T.MEAN(dimension=P)
      T is now of size 1 × R × C
      Compute average T across height (R) and width (C)
     t ← T.MEAN(dimension=(R,C))
      return t
  end procedure
```

3.2.3. Metallurgical and mechanical analysis

To conduct metallurgical analysis a 20×20 mm square was cut out of the single-track walls, situated centrally and 20 mm above the substrate plate (see Fig. 11a). Despite the top of the single-track wall being closer to steady state, the central position was chosen to provide information about the transition in quality of the single-track walls as well as the build stability. The section was mounted and polished to a surface finish of 0.05 μm (see Fig. 11b). The microstructure was made visible by etching with 3% nital. Optical microscopy was conducted using a Hirox KH-8700 up to magnifications of ×1000.

The microscopy revealed a ferritic-pearlitic structure. Sample 4 showed a polygonal ferrite structure with a fine grain size and little to no variation in microstructure when comparing the top and bottom areas of the specimen (see Fig. 12a and b). Sample 11 also shows a consistency in microstructure through the sample, but reveals a larger polygonal ferrite grain size, the presence of acicular ferrite, and pearlite grains as well as the beginning spherodization of pearlite (see Fig. 12c and d). Examining the top and bottom areas of the specimen of sample 14, a difference in microstructure can be seen. The bottom area has notably smaller grains, showing a transition in the microstructure between the two areas (see Fig. 12e and f). Samples 4, 11 and 14 have wall width deviations of 0.141 mm, 0.678 mm and 0.457 mm respectively. This links the quality of the single-track wall to the microstructure of the specimens. A lower wall width deviation yields a finer, more consistent microstructure.

The grain sizes of the samples in the top and bottom areas were measured to the ASTM E-112 standard. This was done in the direction normal to (x) and direction of material accumulation (z), using three images with ×1000 magnification taken on the Hirox KH-8700. Due to the large standard deviation of the results and smaller variation in grain size average, the grain size average cannot be relied upon to give conclusive results. An average of the standard deviations for the top and bottom areas for each sample was used as a t-test (confidence interval 95%) showed no significant statistical difference between the two locations. This was done for grain size measurements in both the x and z directions. Fig. 13a and b shows the wall width deviation plotted against the grain size standard deviation for the x and z grain size measurement directions, respectively. A linear fit onto each data set shows a strong positive correlation between the grain size standard deviation and wall width deviation, with p-values of 0.0016 and 0.0010 and R^2 values of 0.83 and 0.85 in the x and z directions, respectively. This demonstrates a relationship between the wall width variation (build quality) and the variation in grain size of the microstructure in the single-track walls. Additionally, the range in grain size standard deviation for the x direction is 8–14, which is noticeably different to the range 5–22 in the z direction. This is expected, as the larger the wall width variation, the higher the heat as described in Fig. 10. The heat flow is towards the substrate (z direction), and the grain growth is parallel to the heat flow.

Microhardness tests were performed characterising the Vickers Hardness with a 500 g load using a LECO LM 247AT. Indents were made at 2 mm intervals through the centre line of the sample from top to bottom and the standard deviations were calculated. Shown in Fig. 14a, the average hardness (based on 10 measurements, see Fig. 11b) does not vary significantly with wall width deviation. It can be concluded that within the operating parameters, the average hardness of the build does not significantly change. There was also no relationship between hardness and the vertical position of the wall. Instead, the standard deviation of each sample's hardness was plotted against the samples respective wall width deviation, obtaining a p-value of 0.0375 and R^2 value of 0.274 (see Fig. 15a). This shows a positive correlation between the variance of the hardness and the wall with deviation of the single-track walls. As revealed with the microstructure, as the wall width variation increases, the variation in hardness increases. Wall width variation can be used to control the variation in both microstructure and hardness.

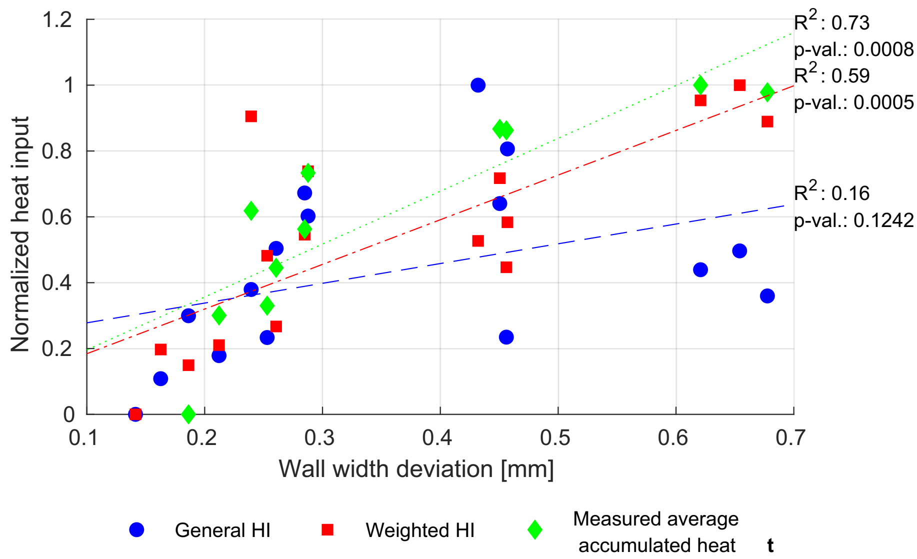

Fig. 10. The correlation between wall width deviation *s*, normalized accumulated heat **t** and calculated heat input.

Images with magnification x600 from the Hirox KH-8700 were processed using the Clemex Vision Lite software to measure the percentage pearlite of the samples in both the top and bottom areas. Five images were analyzed for the top and bottom areas of each sample. A *t*-test was conducted on the top and bottom data for each sample individually. Samples 6, 11, 12, 13, 14, and 16 show a significant differences in percentage pearlite between the top and bottom areas at a confidence level of 95%. Fig. 15b plots the average percentage pearlite against the wall width deviation. The average was obtained from 10 measurements of each sample. A linear regression fit shows a limited tendency for the mean percentage pearlite to increase with increasing wall width deviation with a *p*-value of 0.066 and a quality of fit (R^2) of 0.22. Despite the *p*-value indicating low significance and the low quality of fit, the relationship between the average percentage pearlite and the wall width deviation is still relevant and should not be dismissed entirely.

4. Discussion

The results presented in Section 3.2.1 show that deposition parameters such as WFS and DT, and to a more limited extent the variation in heat extraction represented by the amount of stacked substrate plates results in a significant variation of the wall width deviation. The results particularly show that not including an inter-layer dwell time has a highly significant impact on the wall width deviation. Including a dwell time can reduce the amount of accumulating heat so that the temperature during fabrication can be kept at a desired level. The need for excessive dwell time after each layer can, however, slow down the fabrication process drastically. With the experimental setup used for this work, no active cooling of the substrate plate was available. Through active cooling of the substrate plate, it likely would be possible to achieve similar results in terms of wall width consistency and metallurgical consistency while requiring less dwell time. While the dwell time can be minimized, it is still required as the amount of heat flux towards substrate plate and therefore the cooling rate is limited by the component geometry. It is therefore important to consider a combination of dwell time and active substrate plate cooling to maintain a desired thermal equilibrium.

It was also found in Section 3.2.1 that the parameter TTS does not have a statistically significant influence on the wall width deviation. According to the heat input formulation $Q = \frac{UI}{TTS}$ where U and I are the welding voltage and current, respectively, a decrease in TTS will yield an increased heat input per unit distance. This disagreement can be explained by the chosen envelope for the TTS parameter levels of 0.30 m/min to 0.38 m/min, which was likely too narrow.

In Section 3.2.2, a significant positive correlation between the accumulated heat during fabrication and the wall width deviation is shown. This validates that the amount of heat accumulated during fabrication determines the quality of the single-track wall measured as the wall width deviation. This correlation has also implications on the metallurgical and mechanical properties such as microstructure and hardness.

The microstructure of the samples depends on the thermal cycles, their frequency and intensity. This influenced the heat accumulation and cooling rates of every layer. The thermal cycling of samples 6 and 7 was collected from the IR camera. Shown in Fig. 16b, is the normalized temperature data measured on a vertical line across the centre of the sample after deposition of the last layer (see Fig. 16a). Sample 6 reveals a significantly higher overall temperature than Sample 7. This is a result of the longer dwell times used for Sample 7, where less heat is permitted to accumulate in the build. It should be noted that the temperature in Fig. 16b was normalized with respect to the maximum temperature observed in the temperature data of Sample 6–the sample with the higher overall temperatures.

Evaluating the thermal responses, the frequency and change in cooling rates of the two samples was calculated. The mean cooling rate for sample 6 was 26.51 ± 4.45 C/s and 15.1 ± 3.5 C/s for sample 7. In Fig. 17, the thermal cycles and the derived cooling rate are plotted

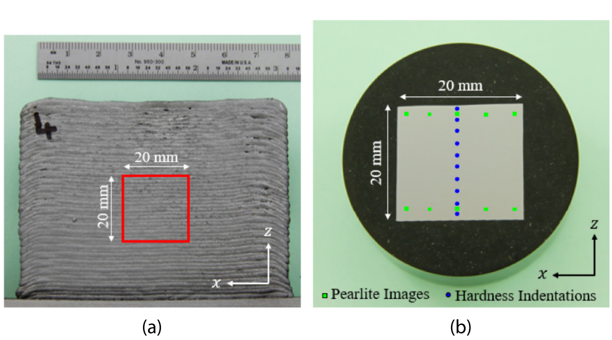

Fig. 11. a) The cut-out square from the centre of the single-track wall and b) the mounted and polished sample.

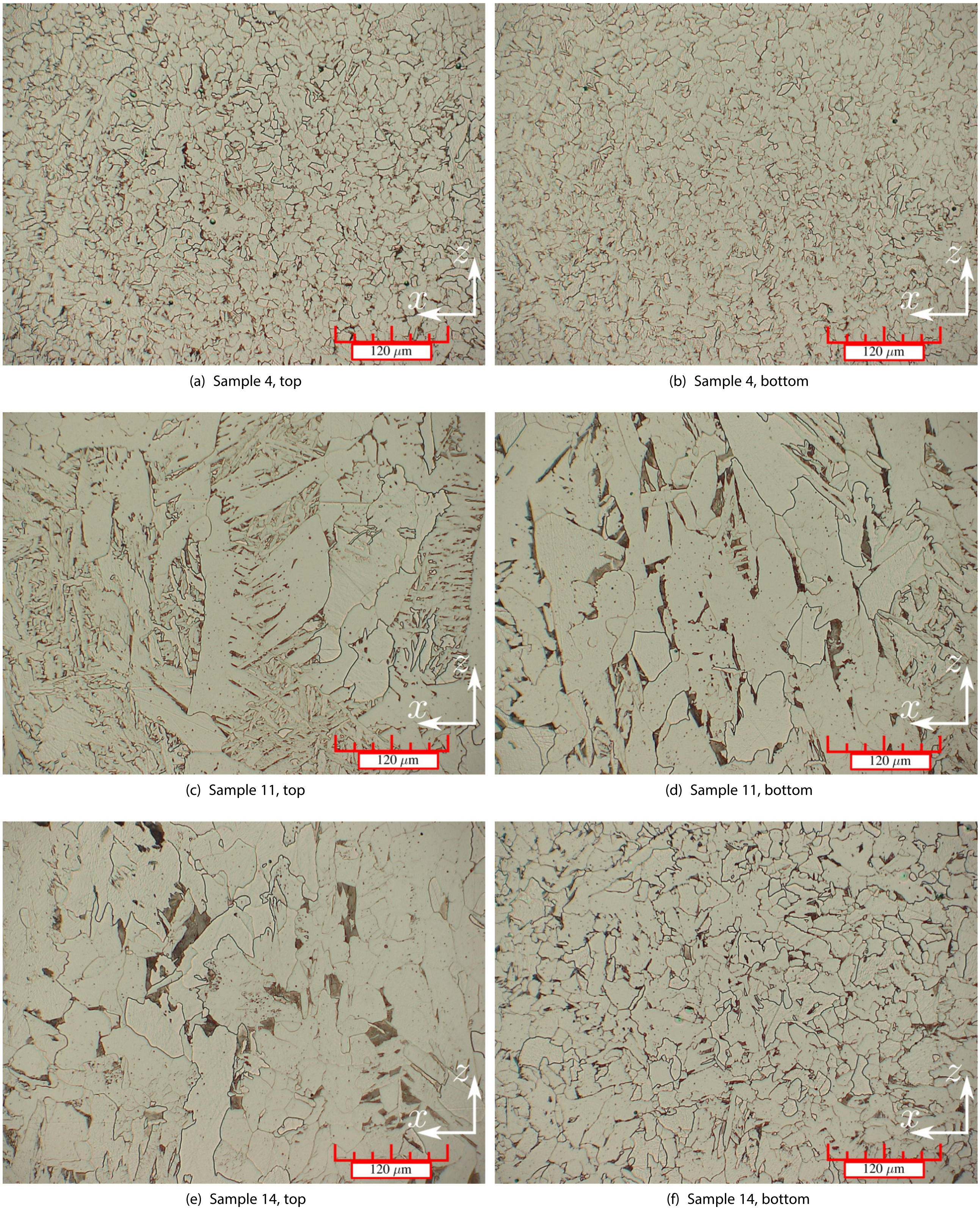

Fig. 12. Micrographs of samples 4, 11 and 14 at ×600 magnification. The micrographs were taken at the top and bottom of the polished sample (see Fig. 11b, green markers).

for sample 6 and 7. The temperature was measured at a single point located at the horizontal centre of the wall and at a vertical distance of 2/5 of the maximum wall height.

A lower WFS resulted in less heat input, lower cooling rates but also lower mean operating temperatures. Slower cooling rates allowed the material time to form a larger percentage Polygonal Ferrite (PF) grains and less Accicular Ferrite (AF) and Coarse Accicular Ferrite (CAF), also known as Widmannstätten Ferrite [45]. It also reduced the the average temperature of the sample, thus allowing less grain growth and a lower tendency to form pearlite (see Fig. 18).

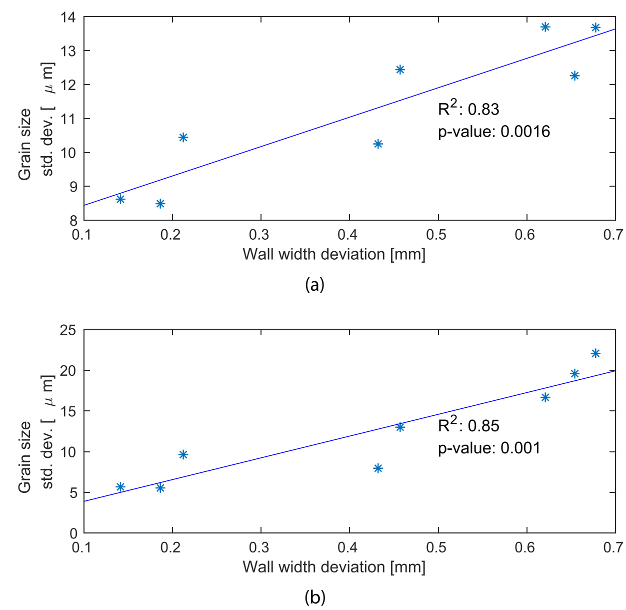

Fig. 13. The grain size standard deviation plotted against the wall width standard deviation measured in a) *x*-direction and b) *z*-direction.

As DT increased, the distinction between the interpass zones increased as can be seen in Fig. 19 with samples 6 and 7, which have the same WFS but DT of 0 and 15 s respectively where Fig. 19b shows a visible distinction between layers creating different microstructures, as opposed to Fig. 19a where with higher energy input the distinction is blurred or non-existent. A DT of 15 s revealed a well defined interpass region between the reheated zones as the material had more time to dissipate heat. This resulted in lower heat accumulation and lower average temperatures, reducing the cooling rate from 26.5 to 15.1 °C/s for samples 6 and 7 respectively as shown in the thermal imaging data, and increasing the percentage of PF present in the sample. Additionally, a lower average temperature produced smaller PF grains, reducing the grain growth.

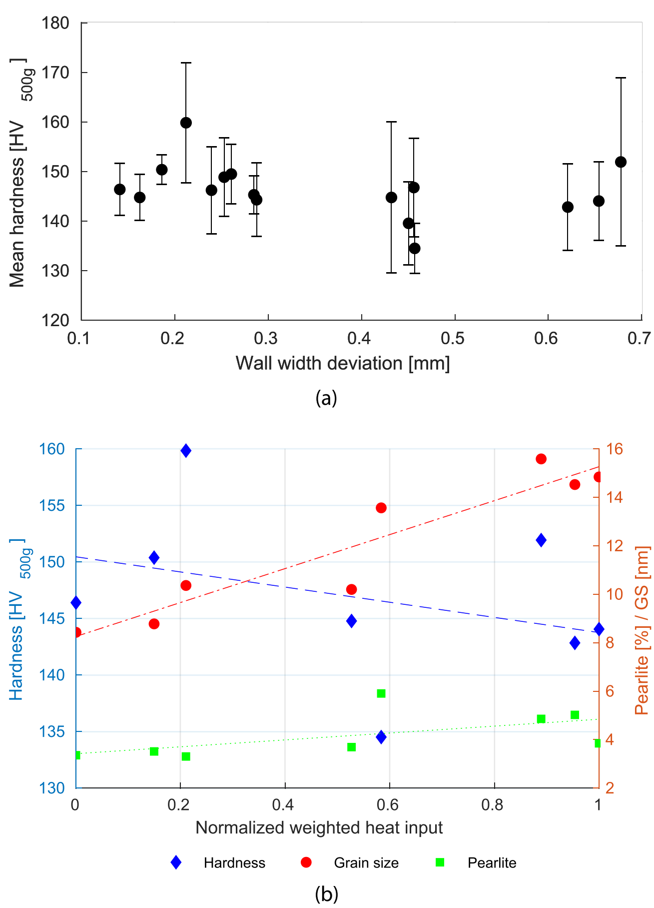

Fig. 14. a) Mean hardness plotted against wall width deviation and b) mean hardness, pearlite % and grain size plotted against the normalized weighted heat input.

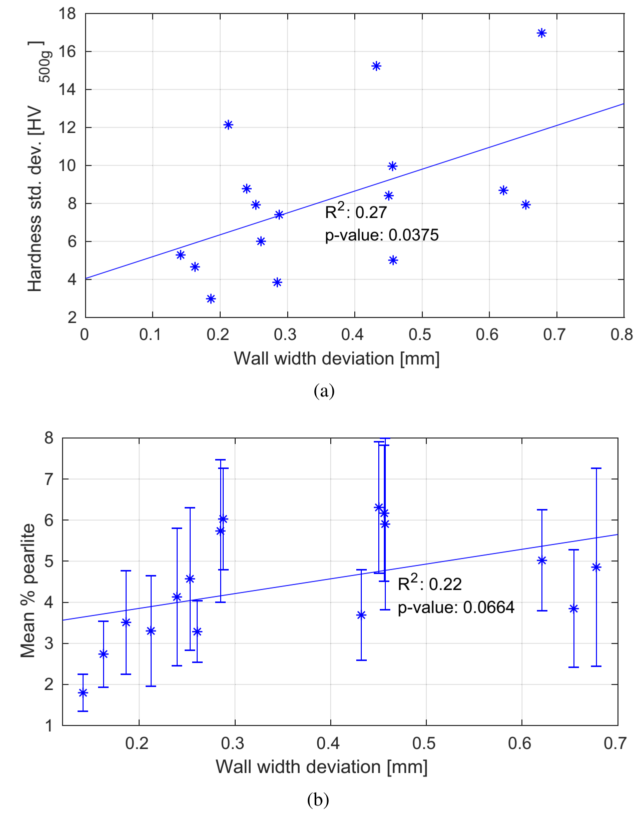

Fig. 15. a) The hardness versus wall width deviation and b) the mean percentage pearlite versus wall width deviation.

Samples with larger wall width deviations had larger grain size deviations (see Fig. 13) due to higher heat input and accumulation (see Fig. 10). As the heat input increased, mean temperature increased, which resulted in grain growth and formation of AC. The result was a larger size difference between the PF and AF as can bee seen in sample 11, as shown in Fig. 12c. As the wall width deviation increased, more heat accumulated faster, resulting in a transition uniform PF and pearlite to a combination of PF, AF and CAF.

The direction of heat input plays a role in the difference in grain size deviation between data taken in the *x*-direction and *z*-direction, with the *z*-direction having a larger range (see Fig. 13). Higher temperatures favour grain growth, and so gains will grow in the direction of heat input, creating a larger grain size deviation in the *z*-direction. As heat input and wall width deviation increase, the grain size deviation increases.

No trends were identified between the microhardness measurements and the distance from the substrate plate of samples 1 through 16. This could be due to the small sample length of 20 mm and large measurement interval of 2 mm used. If tests had been conducted over a larger range of distance on the single-track walls the results may be different. Rodrigues et al. [46] show that a reduction in hardness can be observed across the whole length of the single-track wall as well as large ranges of hardness within 5 mm distances. The cooling rates for

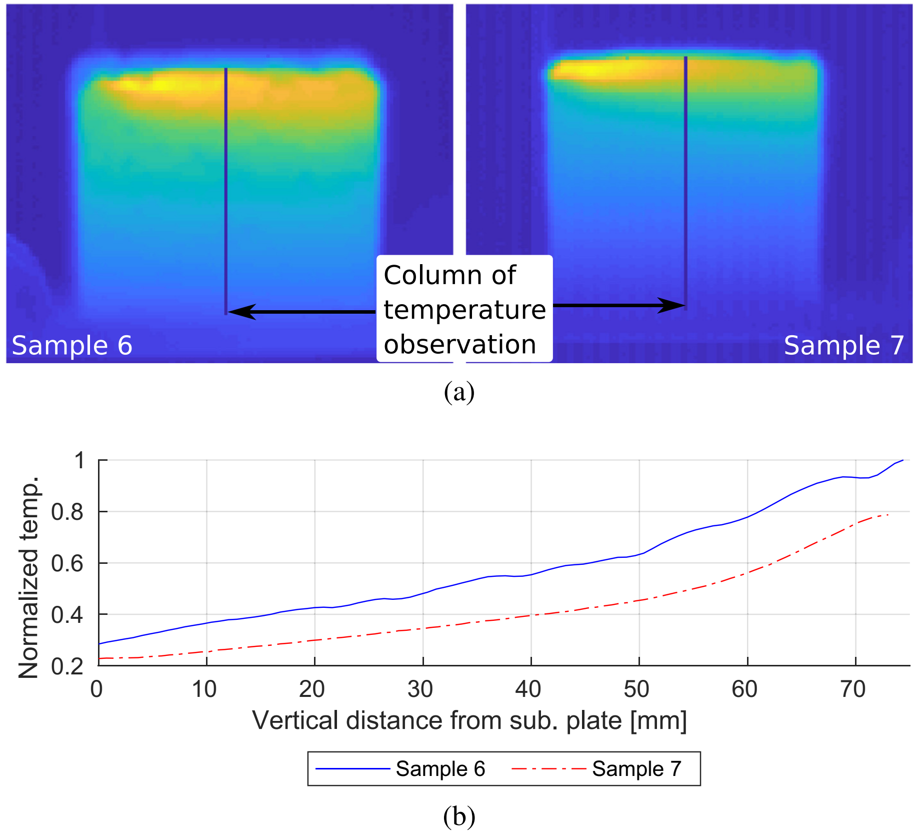

Fig. 16. a) Example IR images for Sample 6 and Sample 7 after the final layer deposition with marked column of temperature observation and b) the normalized temperature measured at the vertical column shown in a) for Sample 6 and Sample 7.

layers formed close to the substrate plate are higher than layers formed half way up the single-track wall. This is due to the substrate plate acting as a heat sink and would suggest the presence of smaller grains, as found in [11]. Consequently, a higher hardness could be found closer to the substrate plate. This effect would be increased by the presence of two substrate plates as shown by the ANOVA analysis (see Table 5).

In summary, the following key observations were made:

1. Heat input is a function of wall width deviation. The larger the heat input, the larger the deviation in wall width.
2. Hardness remains constant within the limits of the build parameters testing in this experiment, however, the variation in hardness does increase with wall width deviation.
3. Grain size is more equiaxed with tighter wall width control.
4. Using a higher degree of wall width control will results in more consistent materials properties.

All aspects of above analysis indicate that microstructure, hardness variations are coupled with the wall width deviation. Wall width deviation in turn is coupled with heat accumulation and deposition parameters. Through minimizing the wall width deviation caused by slumping, it has been shown that the metallurgical variations are also at a minimum.

In general, the process identification and analyses provided in this work demonstrate that the outcome of the AM process is highly coupled in terms of deposition parameter considerations and thermal considerations. Important measures of component properties and quality related to metallurgy and geometry are influenced by the choice of deposition parameters. Advanced AM fabrication processes require the adjustment and in-situ control of the bead and layer geometry, which is achieved by adjusting deposition parameters such as the WFS and TTS. Due to the resulting non-constant deposition parameters during fabrication, the heat input is also not constant. Hence, it is important to account for the variation in heat accumulation by adjusting the extracted heat. There are various common active cooling modalities available such as water or air cooling through which the substrate plate temperature can be feedback controlled as required.

To maintain and control a desired temperature and cooling rate within the component, in-situ temperature monitoring is required. Various temperature sensing modalities such as pyrometers, IR cameras and/or thermocouples can be utilized and combined through sensor fusion to obtain accurate and continuous estimates of the amount of heat, heat flux, the thermal gradient and cooling rate within a component during fabrication.

As mentioned, the amount of heat flux during fabrication is also dependent on the component geometry and therefore not necessarily constant throughout fabrication. As part of process planning, it is therefore necessary to model the fabrication process to predict deposition parameter constraints such that thermal requirements are satisfied given geometry-enforced heat flux limitations.

5. Conclusion & future work

In this work, a detailed and comprehensive analysis of the CMT-based WAAM process is given and factors influencing the quality of the component in terms of geometrical and metallurgical consistency are identified. In particular, it is statistically validated that potentially excessive heat accumulation, which manifests in layer slumping and therefore inconsistent geometry, can be mitigated by the combination of an inter-layer dwell time and adequate heat extraction. The adverse effects of excessive heat input on the microstructure are also shown through establishing a correlation between accumulated heat during fabrication and microstructure variations. Moreover, a strong correlation between the average accumulated heat and the geometrical consistency is shown. A correlation between the grain size deviation and the geometrical consistency is also

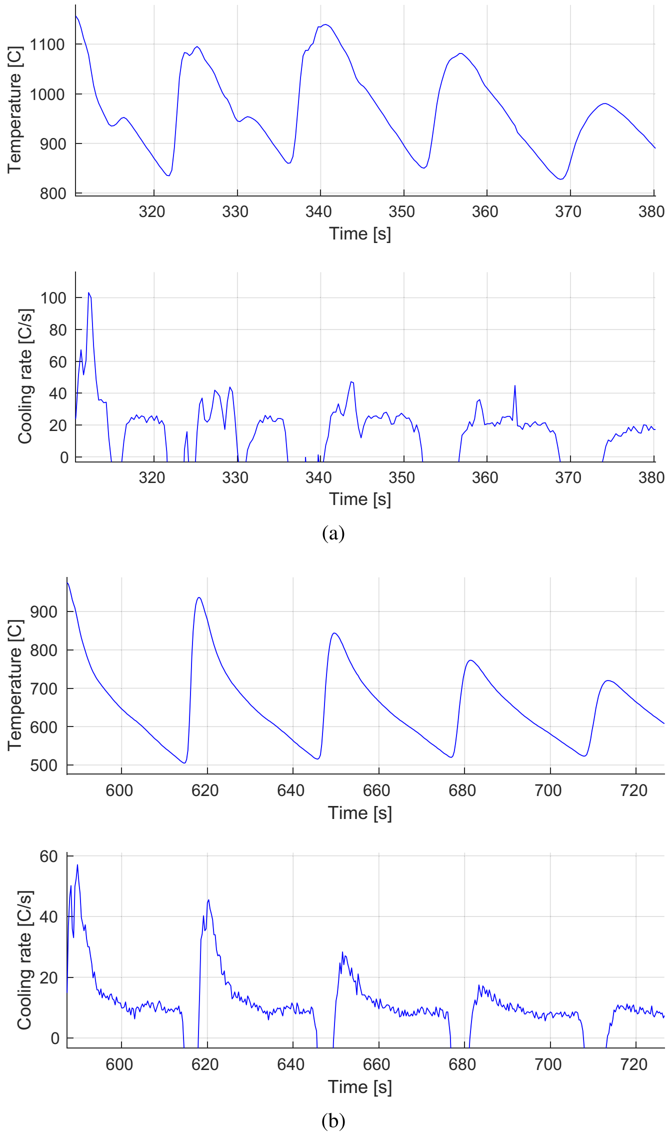

Fig. 17. Thermal cycles (top plot) and cooling rates (bottom plot) for a) sample 6 and b) sample 7 measured at 2/5 of the maximum sample height.

shown, therefore directly linking the geometrical consistency with the accumulated heat during fabrication. In general, the analyses and results presented in this work provide valuable insight into the design considerations and requirements for a large-scale WAAM systems in terms of heat management, sensing and control.

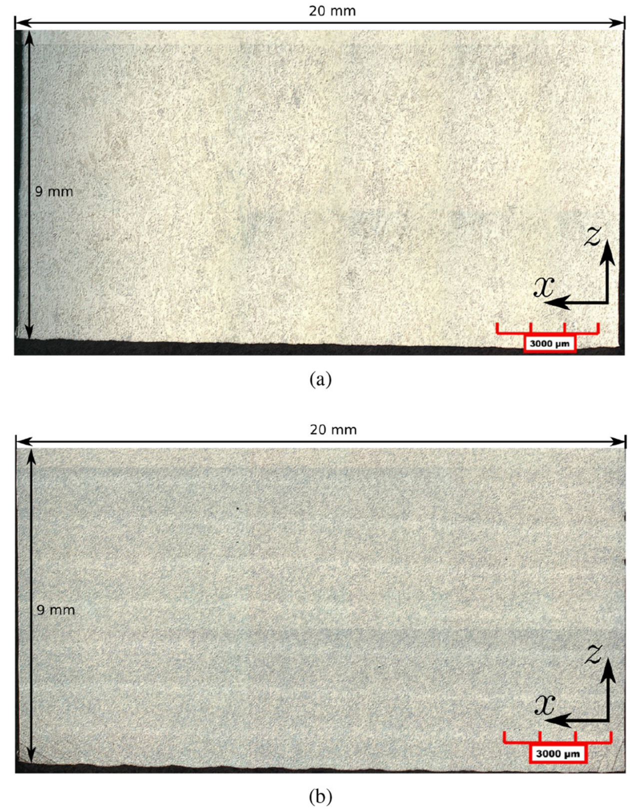

Fig. 19. Micrographs of a) Sample 6 and b) Sample 7 at ×35 magnification and a size of 20×9 mm. The images show the bottom half of each polished wall sample as shown in Fig. 11b.

Our future work will focus on the development of sensor-fusion-based monitoring and control strategies to guarantee a stable fabrication process given the identified constraints in this work and the development of process models for process planning and in-situ prediction thereby informing the above mentioned control strategies

Data availability

The raw/processed data required to reproduce these findings cannot be shared at this time due to technical or time limitations.

CRediT authorship contribution statement

Thomas Lehmann: Writing - original draft, Writing - review & editing, Investigation; Formal analysis; Methodology; Supervision. **Akshay Jain:** Writing - original draft, Data curation, Investigation.

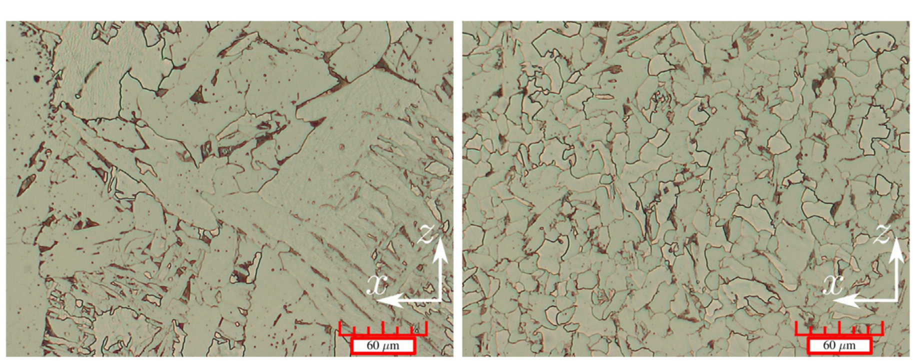

Fig. 18. Micrographs at ×1000 magnification of a) Sample 6 and b) Sample 7.

Yash Jain: Writing - original draft, Writing - review & editing, Formal analysis, Investigation. **Henriette Stainer:** Writing - original draft, Writing - review & editing, Data curation, Formal analysis, Investigation. **Tonya Wolfe:** Writing - original draft, Writing - review & editing, Supervision, Funding acquisition, Investigation. **Hani Henein:** Supervision, Conceptualization. **Ahmed Jawad Qureshi:** Supervision, Conceptualization, Writing - review & editing; Funding acquisition.

Declaration of competing interest

The authors declare that they have no known competing financial interests or personal relationships that could have appeared to influence the work reported in this paper.

Acknowledgements

This work was supported by Mitacs Accelerate (MITACS MA IT11329)

References

[1] Additive manufacturing - ASTM International, [Online]. Available https://www.astm.org/industry/additive-manufacturing-overview.html.
[2] Aurora Labs, [Online]. Available https://auroralabs3d.com/.
[3] Xact metal: accessible, high-caliber 3D metal printing is here, [Online]. Available https://www.xactmetal.com/.
[4] Additive manufacturing machines & materials | GE additive, [Online]. Available https://www.ge.com/additive/.
[5] M. Saunders, Design for metal AM - a beginner's guide, [Online]. Available https://www.renishaw.com/en/design-for-metal-am-a-beginners-guide–43333 2017.
[6] P. Dickens, M. Pridham, R. Cobb, I. Gibson, G. Dixon, Rapid prototyping using 3-D welding, 1992 International Solid Freeform Fabrication Symposium, 1992.
[7] Y.-A. Song, S. Park, S.-W. Chae, 3D welding and milling: part II–optimization of the 3D welding process using an experimental design approach, Int. J. Mach. Tools Manuf. 45 (9) (Jul 2005) 1063–1069.
[8] P. Kazanas, P. Deherkar, P. Almeida, H. Lockett, S. Williams, Fabrication of geometrical features using wire and arc additive manufacture, Proc. Inst. Mech. Eng. B J. Eng. Manuf. 226 (6) (Jun 2012) 1042–1051.
[9] J. Xiong, G. Zhang, W. Zhang, Forming appearance analysis in multi-layer single-pass GMAW-based additive manufacturing, Int. J. Adv. Manuf. Technol. 80 (9–12) (Oct 2015) 1767–1776.
[10] J.L. Prado-Cerqueira, J.L. Diéguez, A.M. Camacho, Preliminary development of a wire and arc additive manufacturing system (WAAM), Procedia Manufacturing 13 (Jan 2017) 895–902.
[11] M. Liberini, A. Astarita, G. Campatelli, A. Scippa, F. Montevecchi, G. Venturini, M. Durante, L. Boccarusso, F.M.C. Minutolo, A. Squillace, Selection of optimal process parameters for wire arc additive manufacturing, Procedia CIRP 62 (Jan 2017) 470–474.
[12] J. González, I. Rodríguez, J.L. Prado-Cerqueira, J.L. Diéguez, A. Pereira, Additive manufacturing with GMAW welding and CMT technology, Procedia Manufacturing 13 (2017) 840–847.
[13] D. Yang, G. Wang, G. Zhang, Thermal analysis for single-pass multi-layer GMAW based additive manufacturing using infrared thermography, J. Mater. Process. Technol. 244 (Jun 2017) 215–224.
[14] X. Lu, Y.F. Zhou, X.L. Xing, L.Y. Shao, Q.X. Yang, S.Y. Gao, Open-source wire and arc additive manufacturing system: formability, microstructures, and mechanical properties, Int. J. Adv. Manuf. Technol. 93 (5–8) (Nov 2017) 2145–2154.
[15] F. Martina, J. Ding, S. Williams, A. Caballero, G. Pardal, L. Quintino, Tandem metal inert gas process for high productivity wire arc additive manufacturing in stainless steel, Additive Manufacturing 25 (Jan 2019) 545–550.
[16] J.D. Spencer, P.M. Dickens, C.M. Wykes, Rapid prototyping of metal parts by three-dimensional welding, Proc. Inst. Mech. Eng. B J. Eng. Manuf. 212 (3) (Mar 1998) 175–182.
[17] Y.M. Zhang, P. Li, Y. Chen, A.T. Male, Automated system for welding-based rapid prototyping, Mechatronics 12 (1) (Feb 2002) 37–53.
[18] Y. Zhang, Y. Chen, P. Li, A.T. Male, Weld deposition-based rapid prototyping: a preliminary study, J. Mater. Process. Technol. 135 (2–3) (Apr 2003) 347–357.
[19] Y.-A. Song, S. Park, D. Choi, H. Jee, 3D welding and milling: part I–a direct approach for freeform fabrication of metallic prototypes, Int. J. Mach. Tools Manuf. 45 (9) (Jul 2005) 1057–1062.
[20] J. Mehnen, J. Ding, H. Lockett, P. Kazanas, Design for wire and arc additive layer manufacture, Global Product Development. 1em Plus 0.5em Minus 0.4em, Springer Berlin Heidelberg, Berlin, Heidelberg 2011, pp. 721–727.
[21] H. Geng, J. Li, J. Xiong, X. Lin, F. Zhang, Optimization of wire feed for GTAW based additive manufacturing, J. Mater. Process. Technol. 243 (May 2017) 40–47.
[22] B. Silwal, M. Santangelo, Effect of vibration and hot-wire gas tungsten arc (GTA) on the geometric shape, J. Mater. Process. Technol. 251 (Jan 2018) 138–145.
[23] O. Yilmaz, A.A. Ugla, Microstructure characterization of SS308LSi components manufactured by GTAW-based additive manufacturing: shaped metal deposition using pulsed current arc, Int. J. Adv. Manuf. Technol. 89 (1–4) (Mar 2017) 13–25.
[24] M. Rafieazad, M. Ghaffari, A. Vahedi Nemani, A. Nasiri, Microstructural evolution and mechanical properties of a low-carbon low-alloy steel produced by wire arc additive manufacturing, Int. J. Adv. Manuf. Technol. 105 (5–6) (2019) 2121–2134.
[25] J.P. Oliveira, T.G. Santos, R.M. Miranda, Revisiting fundamental welding concepts to improve additive manufacturing: from theory to practice, Prog. Mater. Sci. 107 (August 2019) (2020) 100590.
[26] Z. Zeng, B.Q. Cong, J.P. Oliveira, W.C. Ke, N. Schell, B. Peng, Z.W. Qi, F.G. Ge, W. Zhang, S.S. Ao, Wire and arc additive manufacturing of a Ni-rich NiTi shape memory alloy: microstructure and mechanical properties, Additive Manufacturing 32 (September 2019) (2020).
[27] Y. Zhou, X. Lin, N. Kang, W. Huang, J. Wang, Z. Wang, Influence of travel speed on microstructure and mechanical properties of wire + arc additively manufactured 2219 aluminum alloy, J. Mater. Sci. Technol. 37 (2020) 143–153.
[28] P. Almeida, S. Williams, Innovative process model of Ti-6Al-4V additive layer manufacturing using cold metal transfer (CMT), 21st Annual International Solid Freeform Fabrication Symposium 2010, pp. 25–36.
[29] J. Xiong, G. Zhang, H. Gao, L. Wu, Modeling of bead section profile and overlapping beads with experimental validation for robotic GMAW-based rapid manufacturing, Robot. Comput. Integr. Manuf. 29 (2) (Apr 2013) 417–423.
[30] B. Cong, J. Ding, S. Williams, Effect of arc mode in cold metal transfer process on porosity of additively manufactured Al-6.3%Cu alloy, Int. J. Adv. Manuf. Technol. 76 (9–12) (Feb 2015) 1593–1606.
[31] J.S. Panchagnula, S. Simhambhatla, Manufacture of complex thin-walled metallic objects using weld-deposition based additive manufacturing, Robot. Comput. Integr. Manuf. 49 (Feb 2018) 194–203.
[32] F. Li, S. Chen, Z. Wu, Z. Yan, Adaptive process control of wire and arc additive manufacturing for fabricating complex-shaped components, Int. J. Adv. Manuf. Technol. 96 (1–4) (Apr 2018) 871–879.
[33] F. Li, S. Chen, J. Shi, Y. Zhao, In-process control of distortion in wire and arc additive manufacturing based on a flexible multi-point support fixture, Sci. Technol. Weld. Join. 24 (1) (jan 2019) 36–42.
[34] S. Selvi, A. Vishvaksenan, E. Rajasekar, Cold metal transfer (CMT) technology - an overview, Defence Technology 14 (1) (feb 2018) 28–44.
[35] D. Ding, Z. Pan, D. Cuiuri, H. Li, A practical path planning methodology for wire and arc additive manufacturing of thin-walled structures, Robot. Comput. Integr. Manuf. 34 (aug 2015) 8–19.
[36] D. Ding, C. Shen, Z. Pan, D. Cuiuri, H. Li, N. Larkin, S. Van Duin, Towards an automated robotic arc-welding-based additive manufacturing system from CAD to finished part, CAD Computer Aided Design 73 (apr 2016) 66–75.
[37] Y. Ding, R. Dwivedi, R. Kovacevic, Process planning for 8-axis robotized laser-based direct metal deposition system: a case on building revolved part, Robot. Comput. Integr. Manuf. 44 (apr 2017) 67–76.
[38] G. Ma, G. Zhao, Z. Li, W. Xiao, A path planning method for robotic wire and arc additive manufacturing of thin-walled structures with varying thickness, IOP Conference Series: Materials Science and Engineering 470 (1) (2019).
[39] H. Zhao, G. Zhang, Z. Yin, L. Wu, A 3D dynamic analysis of thermal behavior during single-pass multi-layer weld-based rapid prototyping, J. Mater. Process. Technol. 211 (3) (mar 2011) 488–495.
[40] J. Xiong, R. Li, Y. Lei, H. Chen, Heat propagation of circular thin-walled parts fabricated in additive manufacturing using gas metal arc welding, J. Mater. Process. Technol. 251 (jan 2018) 12–19.
[41] F. Montevecchi, G. Venturini, N. Grossi, A. Scippa, G. Campatelli, Heat accumulation prevention in wire-arc-additive-manufacturing using air jet impingement, Manufacturing Letters 17 (aug 2018) 14–18.
[42] Idle time selection for wire-arc additive manufacturing: a finite element-based technique, Additive Manufacturing 21 (may 2018) 479–486.
[43] Y. Ali, P. Henckell, J. Hildebrand, J. Reimann, J. Bergmann, S. Barnikol-Oettler, Wire arc additive manufacturing of hot work tool steel with CMT process, J. Mater. Process. Technol. 269 (jul 2019) 109–116.
[44] M. Braham, M. Van Droogenbroeck, Deep background subtraction with scene-specific convolutional neural networks, 2016 International Conference on Systems, Signals and Image Processing (IWSSIP) May 2016, pp. 1–4.
[45] M. Lomozik, Effect of the welding thermal cycles on the structural changes in the heat affected zone and on its properties in joints welded in low-alloy steels, Weld. Int. 14 (11) (2000) 845–850.
[46] T.A. Rodrigues, V. Duarte, J.A. Avila, T.G. Santos, R.M. Miranda, J.P. Oliveira, Wire and arc additive manufacturing of HSLA steel: effect of thermal cycles on microstructure and mechanical properties, Additive Manufacturing 27 (February) (2019) 440–450.